

# Optical absorption of twisted bilayer graphene with interlayer potential asymmetry

Pilkyung Moon\*

*New York University Shanghai, Pudong, Shanghai, 200120, China*

Young-Woo Son†

*Korea Institute for Advanced Study, Seoul, 130-722, Korea*

Mikito Koshino‡

*Department of Physics, Tohoku University, Sendai, 980-8578, Japan*

(Dated: May 25, 2022)

We investigate the band structure and the optical absorption spectrum of twisted bilayer graphenes with changing interlayer bias and Fermi energy simultaneously. We show that the interlayer bias lifts the degeneracy of the superlattice Dirac point, while the amount of the Dirac point shift is significantly suppressed in small rotation angles, and even becomes opposite to the applied bias. We calculate the optical absorption spectrum in various asymmetric potentials and Fermi energies, and associate the characteristic spectral features with the band structure. The spectroscopic features are highly sensitive to the interlayer bias and the Fermi energy, and widely tunable by the external field effect.

## I. INTRODUCTION

Twisted bilayer graphene (TBG) is a stacked and rotated two-layer graphene with an in-plane rotation angle other than the integer multiples of  $60^\circ$ .<sup>1-3</sup> With decreasing the rotation angle, the misorientation between two lattice periods produces a moiré interference pattern, of which the spatial period widely varies with the rotational alignment.<sup>4</sup> Due to the band-folding by the long-period potential, TBG exhibits a peculiar band structure with a renormalized Fermi velocity and a reduced saddle point energy, which is distinctly different from monolayer graphene and also from regularly-stacked bilayer graphenes.<sup>2,5-13</sup> In addition, the high-quality superlattice potential, which is inherent to the lattice-mismatched stacking of planar crystals, can offer a unique opportunity to investigate the self-similar energy spectrum of charged particles under the simultaneous influences of a periodic potential and a magnetic field.<sup>14-20</sup>

As a superlattice, the optical absorption peak of TBG systematically shift over a wide range of wavelength with the rotation angle, suggesting that this structure is a promising candidate for optoelectronic applications.<sup>21-27</sup> However, the effect of the interlayer bias (i.e., the electrostatic potential difference between layers) on the optical properties of TBGs has not yet been investigated. The interlayer bias has been widely used in the band structure engineering of multilayer graphene systems.<sup>28-33</sup> For TBG, it is reported that the interlayer bias gives rise to some novel properties in the band structure, such as the additional renormalization of Fermi velocity and topologically protected helical modes.<sup>34,35</sup>

The purpose of this work is to reveal the band structure and the optical absorption spectrum of TBGs under interlayer bias and charge doping. The low-energy spectrum of TBG is composed of four Dirac cones originating from monolayer, and the Dirac point (electron-hole band touching point) are relatively shifted in energy by apply-

ing an interlayer bias.<sup>5,34,35</sup> As a rotation angle reduces, however, we find that the Dirac point shift is strongly suppressed and even becomes opposite to the case when the interlayer coupling was absent. In the angle below  $2^\circ$ , the band structure is not simply regarded as the combination of Dirac cones any more, while the band touching at  $K$  and  $K'$  always remains even in the interlayer bias, owing to the  $C_2$  rotation symmetry. We calculate the optical absorption spectra of TBGs for various interlayer biases and Fermi energies, and associate the characteristic absorption peaks and steps with the specific properties in the band structure. We find these spectroscopic features strongly depend on the interlayer bias and the Fermi energy, and thus widely tunable by the external gate electric field.

This paper organizes as follows. Sec. II presents our theoretical methods utilizing a tight-binding Hamiltonian on explicit lattice models of TBGs. In Sec. III, we investigate the band structures of TBGs for various interlayer bias. And in Sec. IV, we discuss the characteristic optical absorption spectrum of TBGs while changing Fermi energy as well as interlayer bias. We conclude in Sec. V.

## II. THEORETICAL METHODS

### A. Atomic structure

In the TBG, the lattice structures of two layers can be commensurate or incommensurate sensitively depending on the rotation angle. However, the basic physical property almost continuously evolves with the period of the moiré interference pattern which continuously varies with the rotation angle.<sup>21</sup> Here we consider three specific commensurate TBG's  $\theta = 9.43^\circ$ ,  $3.89^\circ$ , and  $1.47^\circ$ , which are illustrated in Fig. 1. The dashed (orange) and solid (green) lines represent the lattices of layers 1 and 2. Since the effects of the relative displacement between two lay-

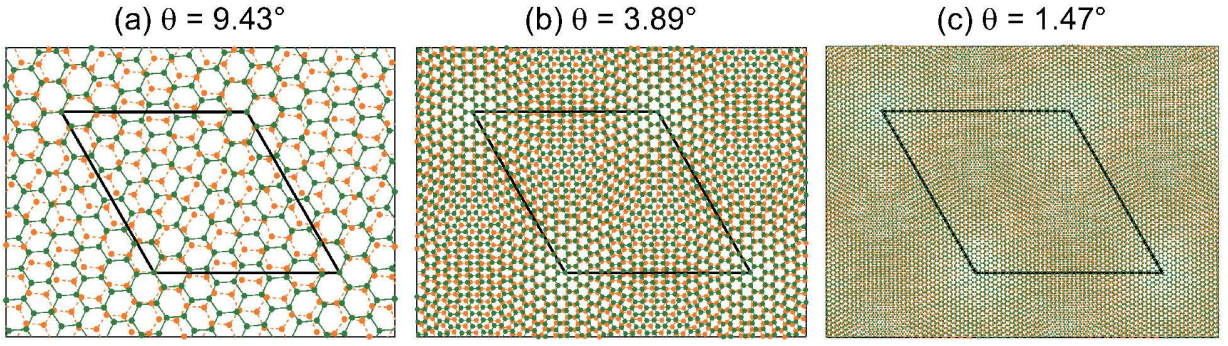


FIG. 1: (Color online) Atomic structures of TBGs with (a)  $\theta = 9.43^\circ$  and (b)  $\theta = 3.89^\circ$ . Dashed (orange) and solid (green) lines represent the lattices of layers 1 and 2, respectively. Black solid lines show the moiré superlattice cell, of which lattice constants are 1.50 nm, 3.62 nm, and 9.59 nm, respectively.

ers on the band structure of TBG are almost negligible,<sup>21</sup> we only consider the structure where the two layers share the atomic position at the center of rotation.

### B. Tight-binding model

In studying the optical properties of TBG, its lattice structures should be included explicitly into the model Hamiltonian to catch the hidden symmetry of the system correctly.<sup>21</sup> To calculate the eigenenergies and eigenfunctions of TBG, we used the single-orbit ( $p_z$ ) tight-binding model, where the hopping integral  $t(\mathbf{R}_i - \mathbf{R}_j)$  between any of two carbon atoms at  $\mathbf{R}_i$  and  $\mathbf{R}_j$  are described by a conventional Slater-Koster formula with three parameters;

$$-t(\mathbf{d}) = V_{pp\pi}(\mathbf{d}) \left[ 1 - \left( \frac{\mathbf{d} \cdot \mathbf{e}_z}{d} \right)^2 \right] + V_{pp\sigma}(\mathbf{d}) \left( \frac{\mathbf{d} \cdot \mathbf{e}_z}{d} \right)^2, \quad (1)$$

where  $V_{pp\pi}(\mathbf{d}) = V_{pp\pi}^0 \exp(-(d - a_0)/\delta_0)$ ,  $V_{pp\sigma}(\mathbf{d}) = V_{pp\sigma}^0 \exp(-(d - d_0)/\delta_0)$ ,  $\mathbf{d} = \mathbf{R}_i - \mathbf{R}_j$ ,  $d = |\mathbf{d}|$ , the nearest intralayer coupling  $V_{pp\pi}^0 \approx -2.7$  eV, the nearest interlayer coupling  $V_{pp\sigma}^0 \approx 0.48$  eV, and the decay length of the hopping integral  $\delta_0 \approx 0.184a$ .<sup>9,36-38</sup> Here,  $a_0 = a/\sqrt{3} \approx 0.142$  nm is the distance of neighboring  $A$  and  $B$  sites on monolayer, and  $d_0 \approx 0.335$  nm is the interlayer spacing. For TBGs, we consider the hopping within  $d < 4a_0$ , while for monolayer,  $AA$ , and  $AB$ , we consider only the nearest neighbor hopping. The Hamiltonian is written as

$$H = - \sum_{\langle i,j \rangle} t(\mathbf{R}_i - \mathbf{R}_j) |\mathbf{R}_i\rangle \langle \mathbf{R}_j| + \sum_i V_i |\mathbf{R}_i\rangle \langle \mathbf{R}_i| + \text{H.c.}, \quad (2)$$

where  $|\mathbf{R}_i\rangle$  represents the atomic state at site  $i$ , and local on-site energy to include an effect of layer-dependent electric potentials in the presence of transverse electric field. For TBG with separate top and bottom gate geometry,<sup>39</sup> the system can be doped with different electric potential

for each layer. We model such a situation with a rigid band approximation while varying  $V_i$ .

### C. Dynamical conductivity

We calculate the dynamical conductivity

$$\sigma_{xx}(\omega) = \frac{e^2 \hbar}{iS} \sum_{\alpha, \beta} \frac{f(\varepsilon_\alpha) - f(\varepsilon_\beta)}{\varepsilon_\alpha - \varepsilon_\beta} \frac{|\langle \alpha | v_x | \beta \rangle|^2}{\varepsilon_\alpha - \varepsilon_\beta + \hbar\omega + i\eta} \quad (3)$$

from the eigenstate  $|\alpha\rangle$  ( $|\beta\rangle$ ) obtained by the tight-binding model. Here, the sum is over all states,  $S$  is the area of the system,  $f(\varepsilon)$  is the Fermi distribution function,  $\varepsilon_\alpha$  ( $\varepsilon_\beta$ ) represents the eigenenergy of the system,  $v_x = -(i/\hbar)[x, H]$  is the velocity operator, and  $\eta$  is the phenomenological broadening which is set to 0.13 meV in the following calculations. A finite broadening factor  $\eta$  is necessary to avoid a singular behavior in the numerical calculation, and here we set it to a sufficiently small value to simulate the nearly ideal system. A different choice of  $\eta$  will change the broadening width of the absorption spectra, are not much sensitive. Actual value of  $\eta$  in the realistic situation depends on the quality of the sample and also on the experimental details. The transmission of light incident perpendicular to a two-dimensional system is given by<sup>40</sup>

$$T = \left| 1 + \frac{2\pi}{c} \sigma_{xx}(\omega) \right|^{-2} \approx 1 - \frac{4\pi}{c} \text{Re} \sigma_{xx}(\omega). \quad (4)$$

## III. BAND STRUCTURES

We calculate the band structure of TBG with the electrostatic potential  $U/2$  and  $-U/2$  applied to the layer 1 and 2, respectively. Figure 2 shows the band structures of TBGs with  $\theta = 9.43^\circ$  and  $3.89^\circ$  at  $U = 0, 0.1, 0.2$  eV, and Fig. 3 shows similar plots for  $\theta = 1.47^\circ$ . We also plot the density of states (DOS) of  $\theta = 3.89^\circ$  in Fig. 2(c). In all the plots, the charge neutrality point is set to 0 eV.

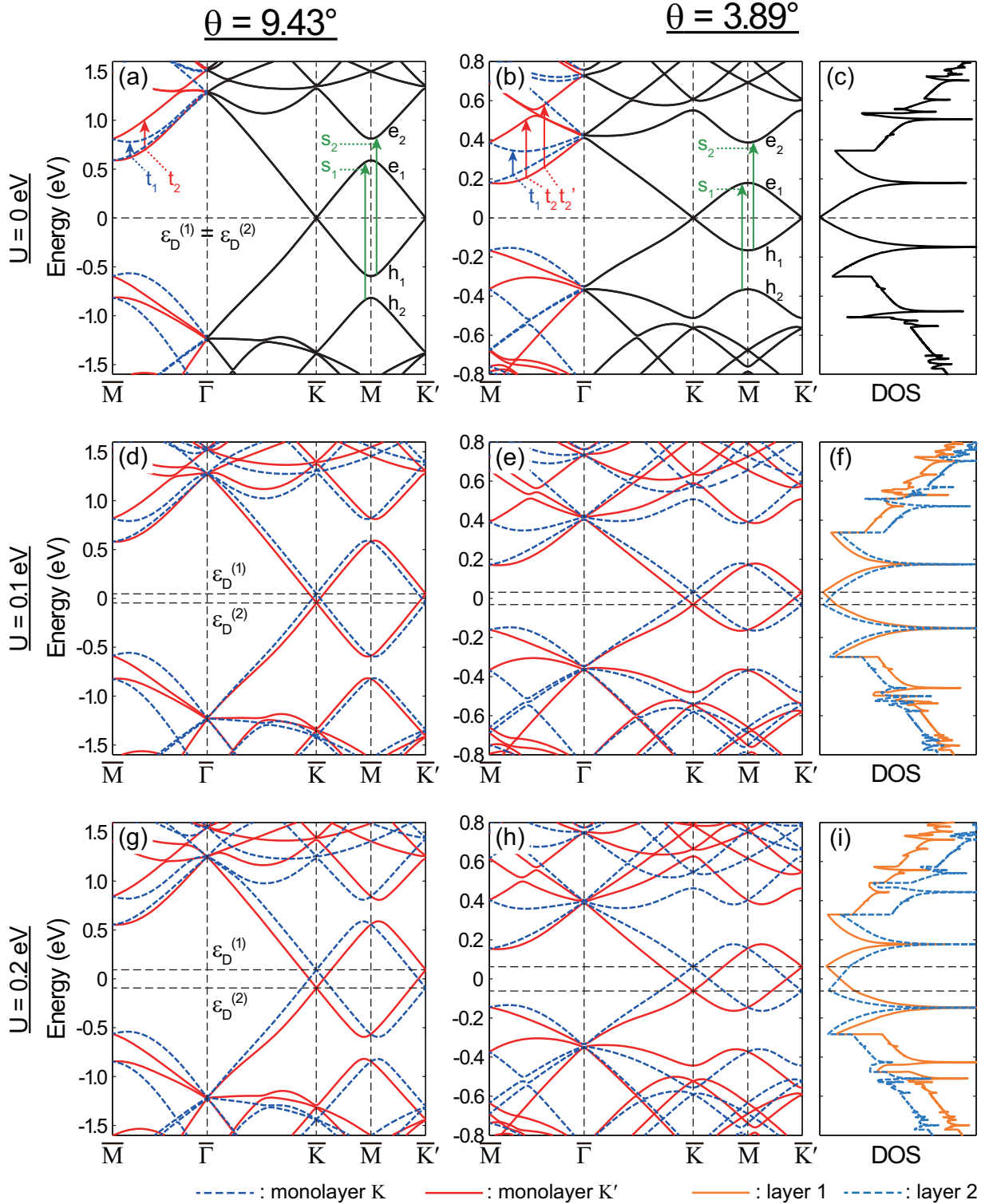


FIG. 2: (Color online) Band structures of TBGs with  $\theta = 9.43^\circ$  [(a), (d), and (g)] and  $\theta = 3.89^\circ$  [(b), (e), and (h)] for different interlayer bias  $U = 0 \text{ eV}$ ,  $U = 0.1 \text{ eV}$ , and  $U = 0.2 \text{ eV}$ . Dashed (blue) and solid (red) lines represent the nearly degenerate branches from the monolayer's  $K$  and  $K'$  region, respectively (see text). (c), (f), and (i) show the DOS of layer 1 (solid orange) and 2 (dashed blue) in  $\theta = 3.89^\circ$  with  $U = 0, 0.1$ , and  $0.2 \text{ eV}$ , respectively.  $\varepsilon_D^{(1)}$  and  $\varepsilon_D^{(2)}$  denote the Dirac point energies of layer 1 and 2.

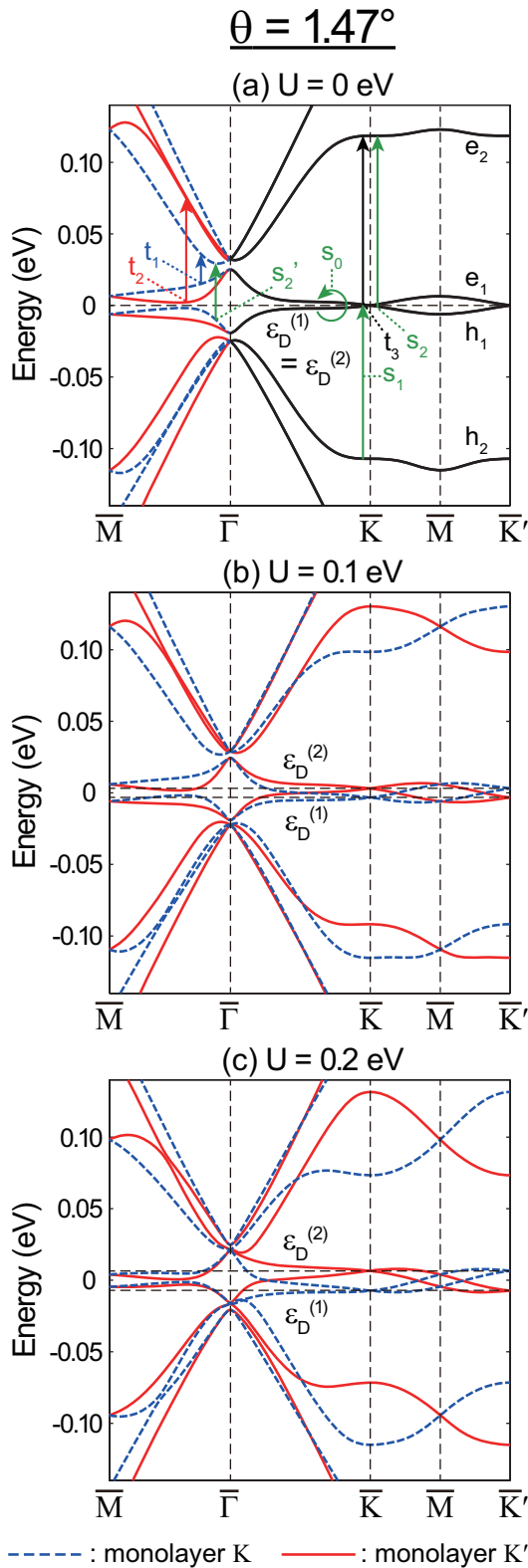


FIG. 3: (Color online) Plots similar for Fig. 2 for TBG with  $\theta = 1.47^\circ$  with different interlayer bias (a)  $U = 0$  eV, (b)  $U = 0.1$  eV, and (c)  $U = 0.2$  eV. Note that the energy shifts of the monolayer's  $K$  and  $K'$  branches with  $U$  are opposite to those of the structures in Fig. 2 (see text).

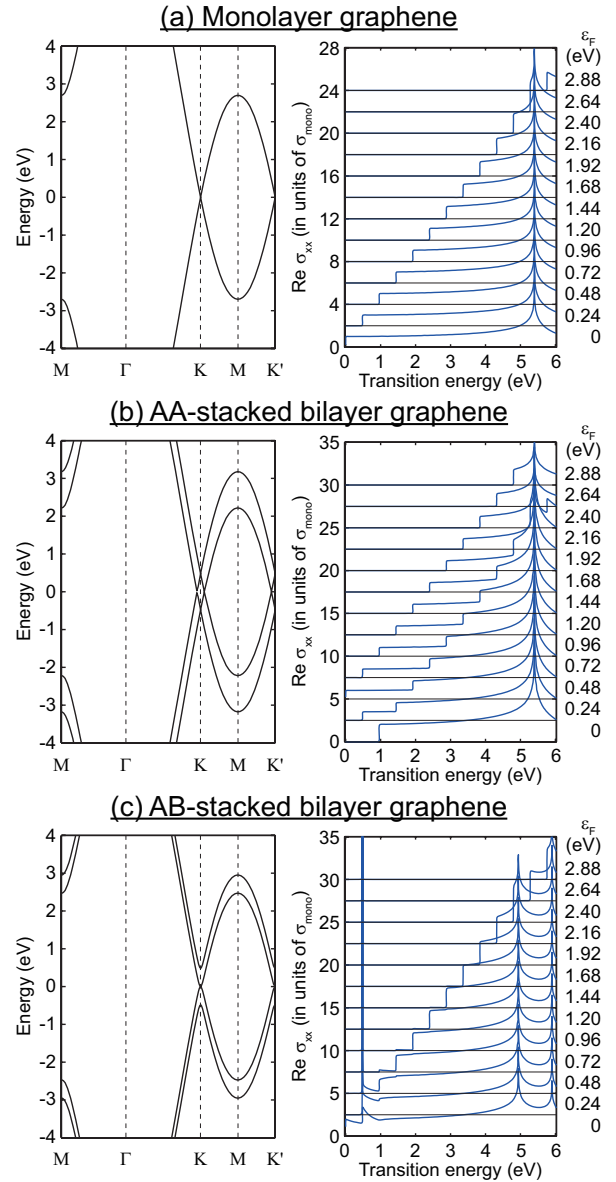


FIG. 4: Band structure (left panel) and dynamical conductivities at various Fermi energies  $\epsilon_F$  (right panel) for (a) monolayer graphene, (b) AA-stacked bilayer graphene, and (c) AB-stacked bilayer graphene.

Four valleys  $K^{(l)}$  and  $K'^{(l)}$  of the layer  $l$  ( $l = 1, 2$ ) are mapped to the two superlattice Dirac points  $\bar{K}$  and  $\bar{K}'$ .<sup>8</sup> In a low-energy regime, a Dirac cone in one layer strongly interacts with only one Dirac cone in another layer, since the other cones are too far separated to be mixed by the slowly varying potential of the superlattice. Thus, each energy band can be classified by the monolayer's valley character, i.e.,  $K$  band from  $K^{(1)}$ - and  $K^{(2)}$ -points, and  $K'$  band from  $K'^{(1)}$ - and  $K'^{(2)}$ -points,<sup>21</sup> while it is folded in the common reduced Brillouin zone. We marked the bands with different colors in Figs. 2(a) and 2(b), according to their original valley characters  $K$  and  $K'$ . These

two bands are mirror symmetric to each other with respect to the lines of  $\bar{K} - \bar{\Gamma}$ ,  $\bar{K}' - \bar{\Gamma}$ , and  $\bar{K} - \bar{K}'$ .<sup>14</sup> For comparison, we plot the band dispersion of monolayer graphene and two forms of regular bilayer graphene, *AA* and *AB*, at the left panels in Figs. 4(a), 4(b), and 4(c), respectively. Compared to the Dirac cones with offset in *AA*, and also to the massive dispersion in *AB*, TBG exhibits monolayerlike dispersion in the vicinity of the charge neutrality point.<sup>2,5</sup>

The low-energy band structure of TBG is composed of the Dirac cones originating from the two monolayer graphenes. Due to the band folding, the band widths of the lowest conduction band ( $e_1$ ) and valence band ( $h_1$ ) of TBG gradually decrease as the rotation angle reduces.<sup>14</sup> As the angle is further reduced, the energy scale of the folded band becomes comparable to the interlayer coupling energy. In  $\theta = 1.47^\circ$  (Fig. 3), the renormalized band velocity is significantly reduced so that a flat band arises near the Dirac point.<sup>5,7-10</sup>

When the interlayer bias  $U$  is introduced, it lifts the degeneracy of the superlattice Dirac point. In large twist angles  $\theta > 10^\circ$ , the energy shift of the Dirac point approximates  $\varepsilon_D^{(l)} \approx \pm U/2$  for layer  $l = 1, 2$ , respectively, as if the two graphene layer were fully decoupled.<sup>5,34,35</sup> This is because in large  $\theta$ , the interlayer coupling is so weak near zero energy that the Dirac cones of two layers remain almost independent. As the rotation angle decreases, however, the energy offset between the two Dirac points is suppressed. For  $U = 0.1$  and  $0.2$  eV, TBG with  $\theta = 9.43^\circ$  shows  $\varepsilon_D^{(1)} = 46.2$  and  $92.3$  meV ( $\approx 8\%$  suppression), while TBG with  $\theta = 3.89^\circ$  shows  $\varepsilon_D^{(1)} = 31.7$  and  $61.5$  meV ( $\approx 38\%$  suppression), respectively. In small  $\theta$ , the energy scale of the folded band becomes comparable to  $|U|$  so that the interlayer band mixing becomes prominent near Dirac points. Thus, the wave function is distributed to both layers, and even at the Dirac point, the layer polarization of the carrier is weakened and the Dirac point shift is decreased. As  $\theta$  further reduces, the shift of Dirac point changes its sign, as can be seen from the negative  $\varepsilon_D^{(1)}$  in Fig. 3(b)-(c).

Using the effective continuum model,<sup>21</sup> the amount of the shift can be approximately estimated as

$$\varepsilon_D^{(1)} = \pm \frac{U (\hbar v q)^2 - 6u_0^2}{2 (\hbar v q)^2 + 6u_0^2}, \quad (5)$$

with  $\pm$  for layer  $l = 1, 2$ , respectively, where  $u_0 \approx 0.11$  eV is the interlayer coupling energy,<sup>21</sup> and  $q = 8\pi \sin(\theta/2)/(3a)$  is the length of the moiré reciprocal lattice vector. This is obtained by a few-mode approximation where only  $k$ -points that directly couple to the Dirac point of layer 1 are taken into account in the effective continuum model.<sup>21</sup> The detail of the derivation is presented in Appendix. Equation (5) stands at large angle  $\theta$  such that  $\hbar v q \gg u_0$ , and also the moderate bias  $|U| \ll u_0$ . The analytic expression shows that the Dirac point shifts monotonically reduces as decreasing  $\theta$  (i.e.,

decreasing  $q$ ), and reaches zero at  $\hbar v q = \sqrt{6}u_0$ , or

$$\theta_c \approx \frac{3\sqrt{6}a}{4\pi\hbar v} u_0 \approx 1.7^\circ. \quad (6)$$

In Fig. 5(a), we plot  $\varepsilon_D^{(1)}$  for  $U = 0.1$  eV calculated by the full-wave effective continuum model, four-wave model [Eq. (A1)], analytic model [Eq. (5)], and tight-binding method. The four models are almost perfectly consistent with each other at  $\theta > 2^\circ$ . We plot  $\varepsilon_D^{(1)}$  at small angle regime in Fig. 5(b). Figures 5(c), (d), and (e) show the band structures from the monolayer's  $K$  valley at  $\theta = 0.62^\circ, 1.47^\circ$ , and  $2.5^\circ$ , respectively, calculated by the effective continuum model. Equation (5) is no longer valid for these cases because the condition  $\hbar v q \gg u_0$  does not hold. In decreasing  $\theta$ , the Dirac point drops below zero at  $\theta \approx 1.7^\circ$ , but again increases and goes to the positive region at  $\theta \approx 1^\circ$ . These features can be reproduced by considering additional six-waves to the four-wave model. As  $\theta$  further reduces from  $\theta = 1^\circ$ , the higher energy bands begin to be mixed to the lowest band, and the energy band is no longer described by the single Dirac cone [Fig. 5(c)]. There the Dirac point energy exhibits a complex oscillatory behavior.

It is somewhat surprising to see that the Dirac points are never gapped even in the presence of the interlayer coupling and the interlayer asymmetric potential. Generally, it is known that the coexistence of the time reversal symmetry and the spatial inversion symmetry requires vanishing of the Berry curvature at any non-degenerate points in the energy band,<sup>41,42</sup> and this guarantees the robustness of band touching points in two-dimensional systems.<sup>43</sup> In a similar manner, we can show that the coexistence of the time reversal symmetry and the in-plane  $C_2$  ( $180^\circ$ ) rotation symmetry (instead of the inversion symmetry) also concludes the same Dirac point protection in two dimensions, because the degree of freedom in  $z$ -direction does not change the argument. The lattice structure of TBG lacks the inversion symmetry but possesses the  $C_2$  symmetry,<sup>14</sup> and moreover,  $C_2$  symmetry holds even in the presence of the interlayer potential asymmetry because  $C_2$  does not flip the layers. This is the origin of the Dirac point protection in the asymmetric TBG. In contrast, *AB*-stacked bilayer graphene has the inversion symmetry but lacks the  $C_2$  symmetry, and thus the band touching is lifted by the interlayer potential difference.<sup>44</sup>

The interlayer band mixing also influences the layer-wise DOS of the biased TBG. In Figs. 2(f) and 2(i), we plot the DOS for layer 1 and 2 by solid (orange) and dashed (blue) lines, respectively. In a fully decoupled bilayer, the DOS of the layer  $l$  should vanish at  $\varepsilon_D^{(l)}$ . Due to the interlayer interaction, however, the layer-wise DOS of the biased TBG does not completely vanishes at the Dirac point of each layer. The minimum of the layer-wise DOS at each layer's Dirac point becomes substantial as the rotation angle reduces or  $|U|$  increases.

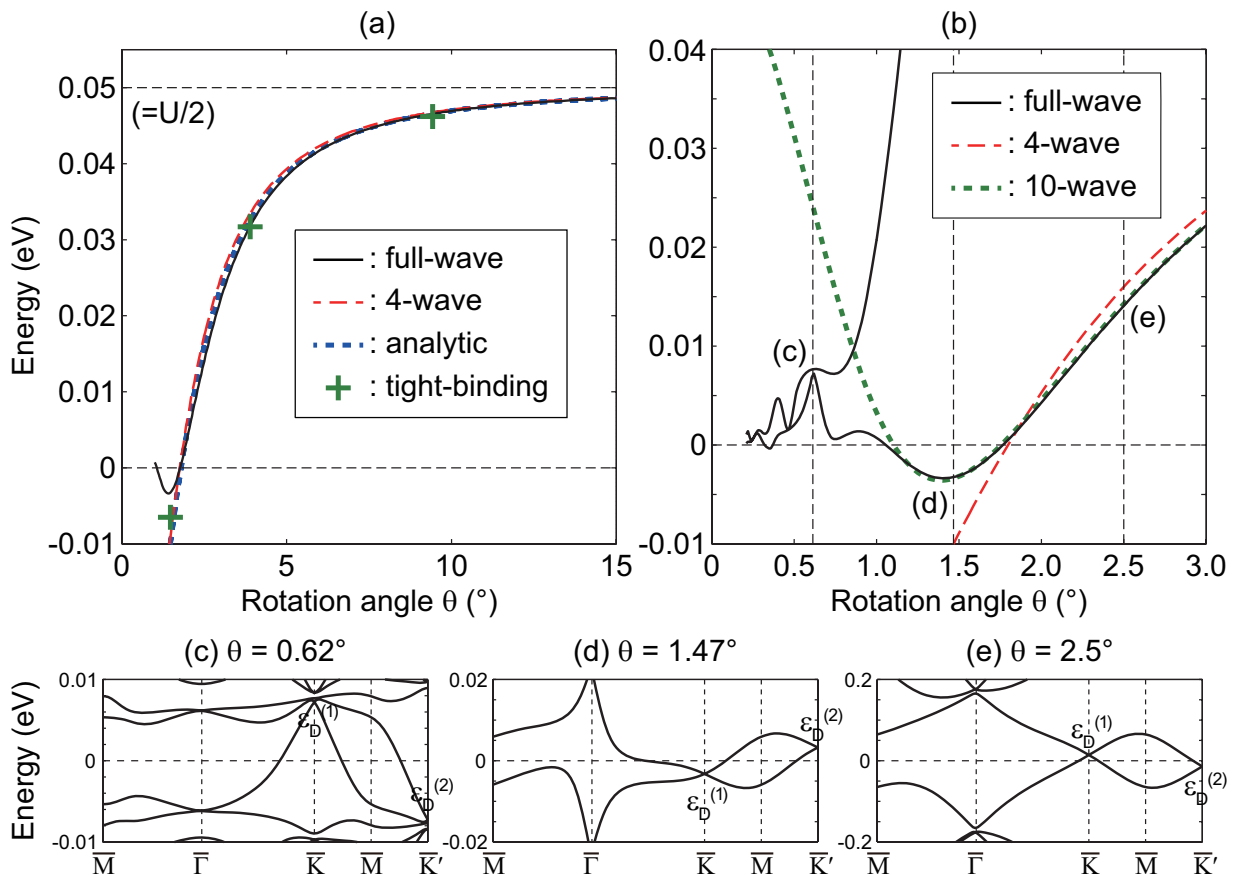


FIG. 5: Dirac point energy  $\varepsilon_D^{(1)}$  of TBG with interlayer bias  $U = 0.1$  eV, as a function of the rotation angle in (a) wide and (b) narrow ranges. In (b), we also plot the higher energy band calculated by the full-wave model. The bottom panels show the band structures (showing only the bands from the monolayer's  $K$  valley) at  $U = 0.1$  eV for (c)  $\theta = 0.62^\circ$ , (d)  $\theta = 1.47^\circ$ , and (e)  $\theta = 2.5^\circ$ , calculated by the effective continuum model.

#### IV. OPTICAL SPECTRUM

We calculated the optical conductivities of the TBGs for various Fermi energies  $\varepsilon_F$  and interlayer asymmetry  $U$ . We plot the optical absorption spectra of TBGs with  $\theta = 9.43^\circ$  for different interlayer bias of  $U = 0, 0.1$ , and  $0.2$  eV in Figs. 6(a), 6(c), and 6(e), respectively. Similar figures for  $\theta = 3.89^\circ$  are presented in Figs. 6(b), 6(d), and 6(f). For comparison, we plot the absorption spectra of monolayer graphene and regular bilayer graphenes ( $AA$ -stack and  $AB$ -stack) at the right panels in Figs. 4(a), 4(b), and 4(c), respectively. When Fermi energy lies at the charge neutrality point ( $\varepsilon_F = 0$ ), the low-energy optical spectrum of monolayer graphene exhibits universal dynamical conductivity

$$\sigma_{\text{mono}} = \frac{g_v g_s e^2}{16 \hbar}, \quad (7)$$

due to the linear dispersion of the band.<sup>45–48</sup> Here  $g_s = 2$  and  $g_v = 2$  are the spin and valley ( $K, K'$ ) degeneracy, respectively. Meanwhile,  $AA$ -stacked bilayer at  $\varepsilon_F = 0$  shows interband absorption step at  $2V_{pp\sigma}^0$ , since Dirac

points are located away from charge neutrality point.<sup>49,50</sup>  $AB$ -stacked bilayer at  $\varepsilon_F = 0$  exhibits absorption edge at  $V_{pp\sigma}^0$  which reflects the interband transition from the low-energy band to the split band.<sup>51–55</sup>

The optical spectrum of TBG is characterized by several unique features described below.

(i) *Interband transition peaks associated with saddle points.* In each panel, we see a characteristic peak near  $1.4$  eV at  $\theta = 9.43^\circ$  and  $0.5$  eV at  $\theta = 3.89^\circ$ . They arise from the interband transitions between the saddle point of the lowest band ( $h_1$  and  $e_1$ ) and the band edge of the second band ( $h_2$  and  $e_2$ ), which are marked as  $s_1$  ( $h_2 \rightarrow e_1$ ) and  $s_2$  ( $h_1 \rightarrow e_2$ ) in Figs. 2(a) and 2(b).<sup>21</sup> Here note that the direct transition between the saddle points ( $h_1 \rightarrow e_1$ ) is forbidden by the selection rule.<sup>21</sup> When  $\varepsilon_F$  is increased to the saddle point, one of the two interband peaks ( $s_1$ ) disappears since the transition to the occupied band  $e_1$  is no longer possible. In increasing  $U$ , on the other hand, we see the interband transition peaks become broad and the intensity gets significantly reduced. This is because, in the presence of  $U$ , the saddle point  $h_1$  ( $e_1$ ) and the band edge  $e_2$  ( $h_2$ ) shift in the

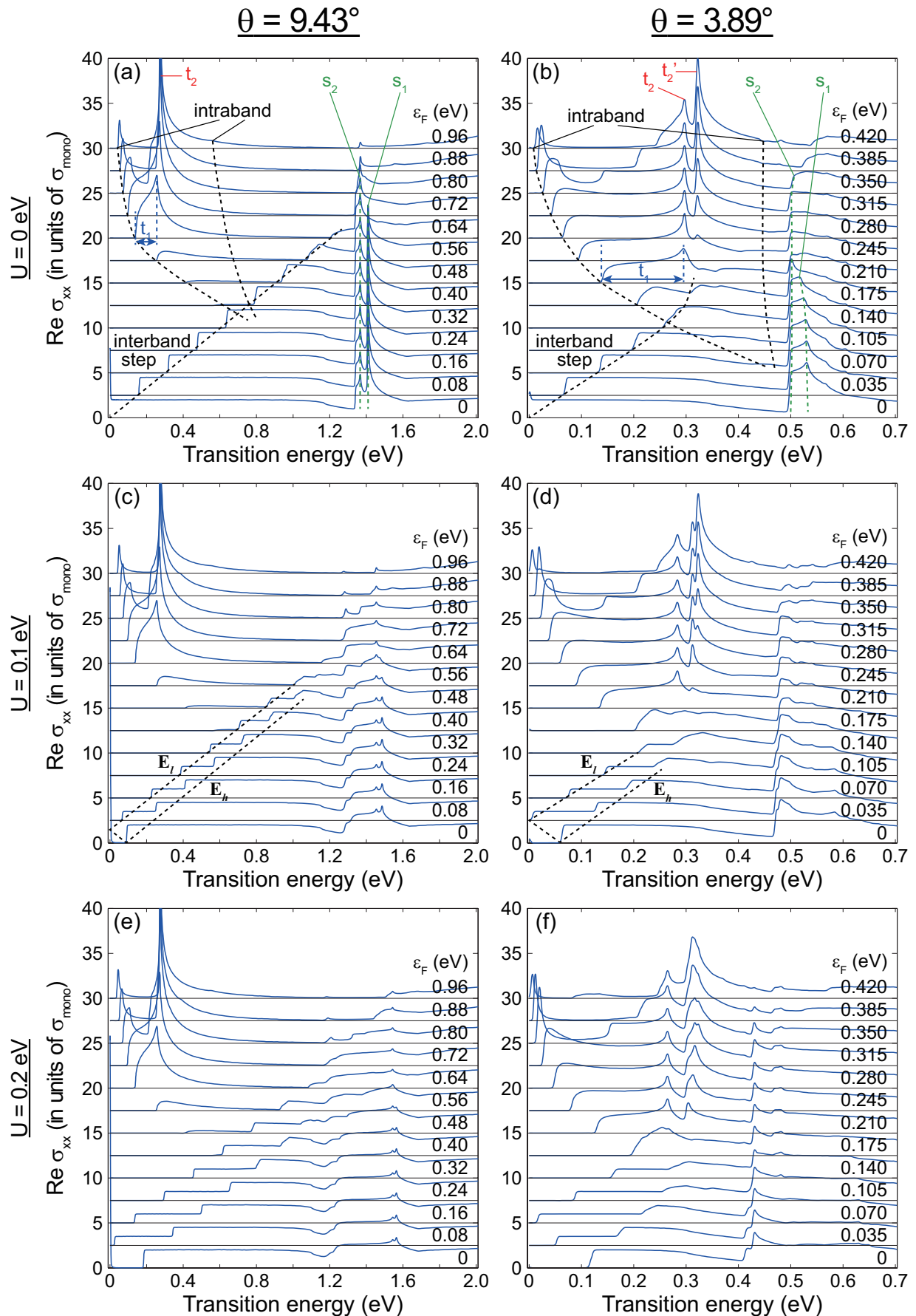


FIG. 6: Dynamical conductivities of TBGs with  $\theta = 9.43^\circ$  with (a)  $U = 0$  eV, (c)  $U = 0.1$  eV, (e)  $U = 0.2$  eV, and  $\theta = 3.89^\circ$  with (b)  $U = 0$  eV, (d)  $U = 0.1$  eV, (f)  $U = 0.2$  eV, for various Fermi energies  $\varepsilon_F$ .

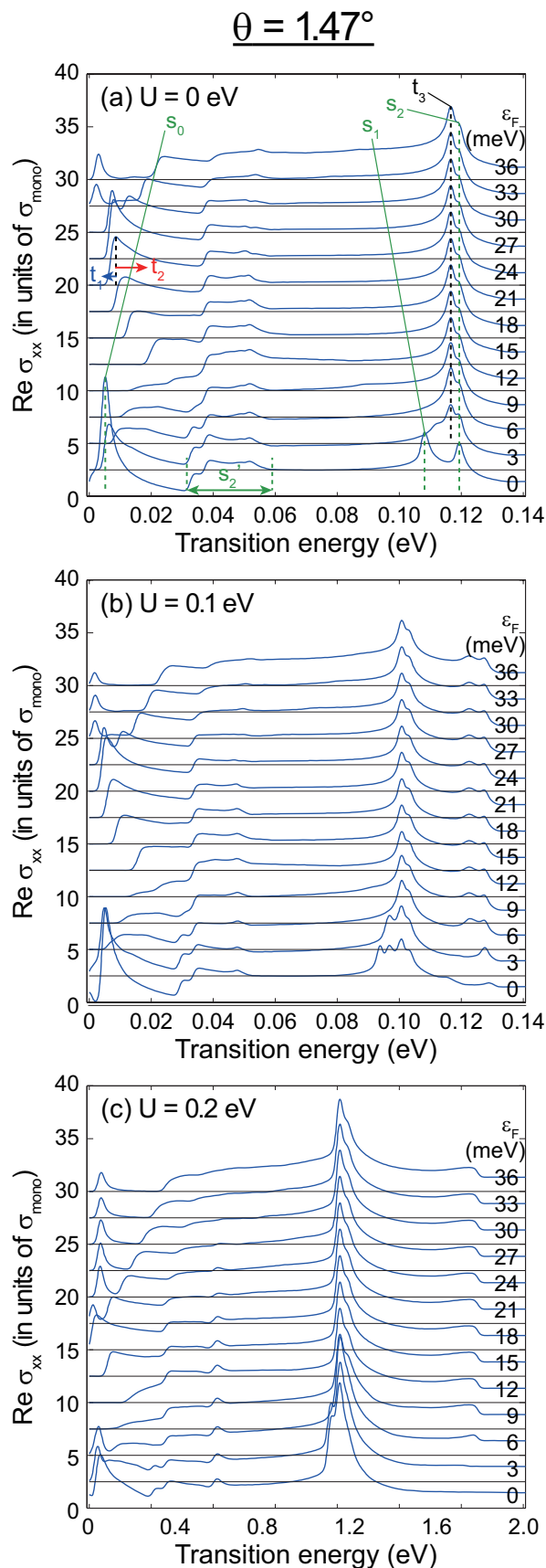


FIG. 7: Plots similar for Fig. 6 for TBG with  $\theta = 1.47^\circ$  with different interlayer bias (a)  $U = 0$  eV, (b)  $U = 0.1$  eV, and (c)  $U = 0.2$  eV for various Fermi energies  $\varepsilon_F$ .

opposite directions as we can see from Fig. 2, and this strongly affects the joint density of states associated with the transition  $s_1$  and  $s_2$ .

(ii) *Interband absorption step.* In the symmetric TBG ( $U = 0$ ) at charge neutral ( $\varepsilon_F = 0$ ), the optical conductivity is close to  $2\sigma_{\text{mono}}$  in the low frequencies. As the Fermi energy  $\varepsilon_F$  deviates from 0, however, we have a discrete step below which the absorption is absent,<sup>26</sup> because the filled electrons forbid the corresponding excitations. The feature is analogous to monolayer graphene [Fig. 4(a)], as it reflects the charging of Dirac cone. The step linearly shifts to higher energies until it vanishes when  $\varepsilon_F$  reaches the saddle point, where the linear dispersion is lost.

In the presence of the asymmetric potential  $U$ , the interband absorption step splits into two different energies

$$\begin{aligned} E_l &= 2|\varepsilon_F - \varepsilon_D^{(1)}|, \\ E_h &= 2|\varepsilon_F - \varepsilon_D^{(2)}|, \end{aligned} \quad (8)$$

due to the relative shift of Dirac point energies  $\varepsilon_D^{(1)}$  and  $\varepsilon_D^{(2)}$ . The step positions  $E_l$  and  $E_h$  linearly depend on  $U$  as expected from Eq. (5). We see similar absorption steps in *AA*-stacked bilayer [Fig. 4(b)],<sup>50</sup> where the Dirac points are originally split at  $U = 0$  by the interlayer coupling energy  $\sim V_{pp\sigma}^0$ . These steps can be moved by the interlayer asymmetry  $U$ , while the shift is just proportional to  $U^2$  unlike in TBG.

(iii) *Intraband absorption peaks.* In the absorption spectrum of charge-doped TBGs ( $\varepsilon_F \neq 0$ ), we see a series of peaks centered at  $\sim 0.3$  eV, which are clearly distinct from those arising from saddle point interband transitions [(i)]. Those peaks reflect the intraband transition  $e_1 \rightarrow e_2$ , which is indicated more specifically as  $t_1$  and  $t_2$  in Figs. 2(a) and 2(b). We see that the two energy bands associated with  $t_2$  are almost parallel between  $\bar{M}$  and  $\bar{\Gamma}$ , where the transition energy is nearly equal to 0.3 eV. This actually causes a sharp absorption peak near 0.3 eV. On the contrary, the transition energy for  $t_1$  significantly depends on wavevector  $k$ , giving a broad absorption peak. In  $\theta = 3.89^\circ$ , the  $t_2$  intraband peak splits into the two peaks at 0.30 eV and 0.32 eV, reflecting the band anti-crossing near the mid-point between  $\bar{M}$  and  $\bar{\Gamma}$ . When the Fermi energy is increased above the saddle point and the second conduction band becomes partially filled, a region with no-absorption appears in the broad  $t_1$  peak, since the transition to the occupied band  $e_2$  becomes forbidden. In increasing the interlayer asymmetry  $U$ , we see that the structure of the intraband transition peak is not considerably changed, in contrast to the significant broadening of the interband transition peaks (i). This is consistent with the fact that the energy dispersion associated the transitions  $t_1$  and  $t_2$  are not strongly modified by  $U$  as we see in Fig. 2.

The optical spectrum of TBG with  $\theta = 1.47^\circ$  is quite different from those of  $\theta > 2^\circ$  due to the significant distortion of the band structure. We plot the optical absorption spectrum of TBG with  $\theta = 1.47^\circ$  for different



interlayer bias of  $U = 0, 0.1, \text{ and } 0.2 \text{ eV}$  in Figs. 7(a), 7(b), and 7(c), respectively. The low-energy spectrum of TBG with  $\theta = 1.47^\circ$  at  $\varepsilon_F = 0$  is characterized by a unique absorption peak near  $5.3 \text{ meV}$ , which is indicated as  $s_0$  in Fig. 3(a). It is the transition between the flat bands that gives a strong absorption peak. The peak suddenly disappears as  $\varepsilon_F$  deviates from charge neutrality point since the band width of  $e_1$  is very narrow. We can also see two characteristic peaks at high-energy spectrum, which arise from the transitions  $s_1$  and  $s_2$  in Fig. 3(a). In TBGs with  $\theta = 9.43^\circ$  and  $3.89^\circ$ , the interband transition peaks (i) occur at  $\bar{M}$  where the band edge of the second band ( $h_2$  and  $e_2$ ) resides there [Figs. 2(a) and 2(b)]. In TBG with  $\theta = 1.47^\circ$ , however, the peaks occur near  $\bar{K}$  and  $\bar{K}'$ , at which the saddle points of the second band reside [Fig. 3(a)]. Likewise with the peak from  $s_0$ ,  $s_1$  also vanishes as  $\varepsilon_F$  deviates from charge neutrality point. However, at that  $\varepsilon_F$ , a new peak from the intraband transition  $t_3$  in Figs. 3(a) and 7(a) is activated at the energy close to  $s_2$ . In increasing the interlayer asymmetry  $U$ , each peak splits into two by the degeneracy lift of the bands (Fig. 3). In increasing  $U$ , the lower-energy peak  $s_1$  gradually redshift and their intensities are significantly enhanced. The spectrum at around  $0.45 \text{ eV}$  originates from the transition near  $\bar{\Gamma}$  [ $s'_2$  in Fig. 3(a)]. The corresponding transitions in TBGs with  $\theta = 9.43^\circ$  and  $3.89^\circ$  have the energy higher than  $s_1$  and  $s_2$ , but in  $\theta = 1.47^\circ$ , it has much smaller energy than  $s_1$  and  $s_2$  due to the band folding. In the low-energy spectrum of charge-doped TBGs ( $\varepsilon_F \neq 0$ ), we see a series of peaks that come from the intraband transitions  $t_1$  and  $t_2$  in Fig. 3(a).

## V. CONCLUSION

We investigated the band structure and the optical absorption spectrum of TBGs with varying interlayer bias and Fermi energies theoretically. We showed that the interlayer bias lifts the degeneracy of the superlattice Dirac point, while the shift of the Dirac point is significantly suppressed as the interlayer rotation angle  $\theta$  reduces. The low-energy band structure including the Dirac point shift was analytically described by the effective

continuum model. We calculated the optical absorption spectrum and associate the characteristic spectral features with the band structure. The spectrum consists of the interband and intraband transition peaks as well as the interband absorption steps, where the peak (step) positions and amplitudes are highly sensitive to the interlayer bias and the Fermi energy. Meanwhile, we showed that both the band structure and optical spectrum of TBG with  $\theta = 1.47^\circ$  quite different from those of  $\theta > 2^\circ$ , due to the strong band distortion caused by interlayer coupling at the low-energy regime. Our calculation results as well as analysis can clarify optical spectrum of TBGs in actual experimental setups such as TBGs on top of different layered materials or the systems in field effect transistor geometries.

## ACKNOWLEDGEMENTS

P. M. was supported by New York University Shanghai (research funds) and East China Normal University (research facilities). Y.-W. S. was supported by the NRF of Korea grant funded by the MSIP (CASE, 2011-0031640 and QMMRC, NO. R11-2008-053-01002-0). M. K. is funded by JSPS Grant-in-Aid for Scientific Research No. 24740193, No. 25107005. Computations were supported by the CAC of KIAS.

## Appendix A: Derivation of the Dirac point shift

Here we derive an approximate analytic expression Eq. (5) for the energy shift of the Dirac points in the TBG under a asymmetric potential. We adopt the effective continuum model,<sup>21</sup> and construct the Hamiltonian only taking account of the  $k$ -points that directly couple to the Dirac point of layer 1,  $\mathbf{K}_\xi^{(1)}$  ( $\xi = \pm 1$  for monolayer's  $K$  and  $K'$ , respectively). In the effective model, the monolayer state of the layer 1 at  $\mathbf{k}$  couples to the state of the layer 2 at  $\mathbf{k}, \mathbf{k} - \xi \mathbf{G}_1^M - \xi \mathbf{G}_2^M$ , and  $\mathbf{k} - \xi \mathbf{G}_2^M$ , where  $\mathbf{G}_1^M$  and  $\mathbf{G}_2^M$  are moiré reciprocal vectors, by the Fourier component of the moiré superlattice potential. The reduced Hamiltonian of the four-wave approximation becomes

$$H_{\text{eff}}(\mathbf{k}) = \begin{pmatrix} H_\xi^{(1)}(\mathbf{k}) + U/2 & U_1^\dagger & U_2^\dagger & U_3^\dagger \\ U_1 & H_\xi^{(2)}(\mathbf{k}) - U/2 & 0 & 0 \\ U_2 & 0 & H_\xi^{(2)}(\mathbf{k} - \xi \mathbf{G}_1^M - \xi \mathbf{G}_2^M) - U/2 & 0 \\ U_3 & 0 & 0 & H_\xi^{(2)}(\mathbf{k} - \xi \mathbf{G}_2^M) - U/2 \end{pmatrix}, \quad (\text{A1})$$

with

$$\begin{aligned} H_\xi^{(l)}(\mathbf{k}) &= -\hbar v(\mathbf{k} - \mathbf{K}_\xi^{(l)}) \cdot \boldsymbol{\sigma}, \\ U_1 &= u_0 \begin{pmatrix} 1 & 1 \\ 1 & 1 \end{pmatrix}, \\ U_2 &= u_0 \begin{pmatrix} 1 & \omega^{-\xi} \\ \omega^\xi & 1 \end{pmatrix}, \\ U_3 &= u_0 \begin{pmatrix} 1 & \omega^{-\xi} \\ \omega^\xi & 1 \end{pmatrix}, \end{aligned}$$

where  $\mathbf{K}_\xi^{(l)}$  is the Dirac point of the layer  $l$ ,  $\boldsymbol{\sigma} = (\sigma_x, \sigma_y)$  is the Pauli matrices,  $u_0 \approx 0.11 \text{ eV}$  represents the in-plane

Fourier component of the interlayer transfer integral, and  $\omega = \exp(2\pi i/3)$ . For a moderate bias such that  $\varepsilon_D^{(1)} \leq -U/2 + \hbar v q$ , where  $|q| = |\mathbf{K}_\xi^{(1)} - \mathbf{K}_\xi^{(2)}| = |\mathbf{G}_1^M|/\sqrt{3} \approx 8\pi \sin(\theta/2)/(3a)$ , the secular equation  $\det(E - H_{\text{eff}}(\mathbf{k})) = 0$  at  $\mathbf{k} = \mathbf{K}_\xi^{(1)}$  is reduced to

$$E - \frac{U}{2} = \frac{6u_0^2}{(E + U/2)^2 - (\hbar v q)^2} \left(E + \frac{U}{2}\right). \quad (\text{A3})$$

Assuming also  $6u_0^2 \gg E^2, U^2/4$  for a moderate bias, the Eq. (A3) finally gives an analytic expression Eq. (5).

- 
- \* Electronic address: pilkyung.moon@nyu.edu  
† Electronic address: hand@kias.re.kr  
‡ Electronic address: koshino@cmpt.phys.tohoku.ac.jp
- <sup>1</sup> J. Hass, R. Feng, J. Millan-Otoya, X. Li, M. Sprinkle, P. First, W. De Heer, E. Conrad, and C. Berger, *Phys. Rev. B* **75**, 214109 (2007).
  - <sup>2</sup> J. Hass, F. Varchon, J. Millan-Otoya, M. Sprinkle, N. Sharma, W. de Heer, C. Berger, P. First, L. Magaud, and E. Conrad, *Phys. Rev. Lett.* **100**, 125504 (2008).
  - <sup>3</sup> A. Luican, G. Li, A. Reina, J. Kong, R. Nair, K. Novoselov, A. Geim, and E. Andrei, *Phys. Rev. Lett.* **106**, 126802 (2011).
  - <sup>4</sup> K. Hermann, *J. Phys.: Condens. Matter* **24**, 314210 (2012).
  - <sup>5</sup> J. Lopes dos Santos, N. Peres, and A. Castro Neto, *Phys. Rev. Lett.* **99**, 256802 (2007).
  - <sup>6</sup> Z. Ni, Y. Wang, T. Yu, Y. You, and Z. Shen, *Phys. Rev. B* **77**, 235403 (2008).
  - <sup>7</sup> E. Morell, J. Correa, P. Vargas, M. Pacheco, and Z. Barticevic, *Phys. Rev. B* **82**, 121407 (2010).
  - <sup>8</sup> S. Shallcross, S. Sharma, E. Kandelaki, and O. Pankratov, *Phys. Rev. B* **81**, 165105 (2010).
  - <sup>9</sup> G. Trambly de Laissardière, D. Mayou, and L. Magaud, *Nano Lett.* **10**, 804 (2010).
  - <sup>10</sup> R. Bistritzer and A. MacDonald, *Proc. Natl. Acad. Sci.* **108**, 12233 (2011).
  - <sup>11</sup> I. Brihuega, P. Mallet, H. González-Herrero, G. Trambly de Laissardière, M. Ugeda, L. Magaud, J. Gómez-Rodríguez, F. Ynduráin, and J.-Y. Veuillen, *Phys. Rev. Lett.* **109**, 196802 (2012).
  - <sup>12</sup> K. Sato, R. Saito, C. Cong, T. Yu, and M. S. Dresselhaus, *Phys. Rev. B* **86**, 125414 (2012).
  - <sup>13</sup> J. D. Correa, M. Pacheco, and E. S. Morell, *J. Mat. Sci.* **49**, 642 (2014).
  - <sup>14</sup> P. Moon and M. Koshino, *Phys. Rev. B* **85**, 195458 (2012).
  - <sup>15</sup> P. Moon and M. Koshino, *Phys. Rev. B* **88**, 241412 (2013).
  - <sup>16</sup> R. Bistritzer and A. MacDonald, *Phys. Rev. B* **84**, 035440 (2011).
  - <sup>17</sup> Z. Wang, F. Liu, and M. Chou, *Nano Lett.* **12**, 3833 (2012).
  - <sup>18</sup> C. Dean, L. Wang, P. Maher, C. Forsythe, F. Ghahari, Y. Gao, J. Katoch, M. Ishigami, P. Moon, M. Koshino, et al., *Nature* **497**, 598 (2013).
  - <sup>19</sup> B. Hunt, J. Sanchez-Yamagishi, A. Young, M. Yankowitz, B. LeRoy, K. Watanabe, T. Taniguchi, P. Moon, M. Koshino, P. Jarillo-Herrero, et al., *Science* **340**, 1427 (2013).
  - <sup>20</sup> L. Ponomarenko, R. Gorbachev, G. Yu, D. Elias, R. Jalil, A. Patel, A. Mishchenko, A. Mayorov, C. Woods, J. Wallbank, et al., *Nature* **497**, 594 (2013).
  - <sup>21</sup> P. Moon and M. Koshino, *Phys. Rev. B* **87**, 205404 (2013).
  - <sup>22</sup> Y. Wang, Z. Ni, L. Liu, Y. Liu, C. Cong, T. Yu, X. Wang, D. Shen, and Z. Shen, *ACS Nano* **4**, 4074 (2010).
  - <sup>23</sup> T. Stauber, P. San-Jose, and L. Brey, *New. J. Phys.* **15**, 113050 (2013).
  - <sup>24</sup> R. W. Havener, C.-J. Kim, L. Brown, J. W. Kevek, J. D. Sleppy, P. L. McEuen, and J. Park, *Nano Lett.* **13**, 3942 (2013).
  - <sup>25</sup> R. W. Havener, Y. Liang, L. Brown, L. Yang, and J. Park, *Nano Lett.* **14**, 3353 (2014).
  - <sup>26</sup> C. J. Tabert and E. J. Nicol, *Phys. Rev. B* **87**, 121402 (2013).
  - <sup>27</sup> Y. Liang, R. Soklaski, S. Huang, M. W. Graham, R. Havener, J. Park, and L. Yang, *Phys. Rev. B* **90**, 115418 (2014).
  - <sup>28</sup> E. McCann, *Phys. Rev. B* **74**, 161403 (2006).
  - <sup>29</sup> E. Castro, K. Novoselov, S. Morozov, N. Peres, J. M. B. Lopes dos Santos, J. Nilsson, F. Guinea, A. Geim, and A. Neto, *Phys. Rev. Lett.* **99**, 216802 (2007).
  - <sup>30</sup> M. Koshino and E. McCann, *Phys. Rev. B* **79**, 125443 (2009).
  - <sup>31</sup> K. F. Mak, C. H. Lui, J. Shan, and T. F. Heinz, *Phys. Rev. Lett.* **102**, 256405 (2009).
  - <sup>32</sup> Y. Zhang, T.-T. Tang, C. Girit, Z. Hao, M. C. Martin, A. Zettl, M. F. Crommie, Y. R. Shen, and F. Wang, *Nature* **459**, 820 (2009).
  - <sup>33</sup> E. Castro, K. Novoselov, S. Morozov, N. Peres, J. Lopes dos Santos, J. Nilsson, F. Guinea, A. Geim, and A. Castro Neto, *J. Phys.: Condens. Matter* **22**, 175503 (2010).
  - <sup>34</sup> L. Xian, S. Barraza-Lopez, and M. Chou, *Phys. Rev. B* **84**, 075425 (2011).
  - <sup>35</sup> P. San-Jose and E. Prada, *Phys. Rev. B* **88**, 121408 (2013).
  - <sup>36</sup> T. Nakanishi and T. Ando, *J. Phys. Soc. Jpn.* **70**, 1647 (2001).
  - <sup>37</sup> S. Uryu, *Phys. Rev. B* **69**, 075402 (2004).
  - <sup>38</sup> J. Slater and G. Koster, *Phys. Rev.* **94**, 1498 (1954).
  - <sup>39</sup> J. Nilsson, A. Neto, F. Guinea, and N. Peres, *Phys. Rev. B* **76**, 165416 (2007).
  - <sup>40</sup> T. Ando, *J. Phys. Soc. Jpn.* **38**, 989 (1975).
  - <sup>41</sup> F. Haldane, *Phys. Rev. Lett.* **93**, 206602 (2004).
  - <sup>42</sup> L. Fu and C. L. Kane, *Phys. Rev. B* **76**, 045302 (2007).
  - <sup>43</sup> M. Koshino, *Phys. Rev. B* **88**, 115409 (2013).
  - <sup>44</sup> E. McCann and V. I. Fal'ko, *Phys. Rev. Lett.* **96**, 086805 (2006).
  - <sup>45</sup> R. Nair, P. Blake, A. Grigorenko, K. Novoselov, T. Booth, T. Stauber, N. Peres, and A. Geim, *Science* **320**, 1308 (2008).
  - <sup>46</sup> T. Ando, Y. Zheng, and H. Suzuura, *J. Phys. Soc. Jpn.* **71**, 1318 (2002).
  - <sup>47</sup> V. Gusynin and S. Sharapov, *Phys. Rev. B* **73**, 245411

- (2006).
- <sup>48</sup> V. Gusynin, S. Sharapov, and J. Carbotte, Phys. Rev. Lett. **96**, 256802 (2006).
- <sup>49</sup> Y. Xu, X. Li, and J. Dong, Nanotechnology **21**, 065711 (2010).
- <sup>50</sup> C. J. Tabert and E. J. Nicol, Phys. Rev. B **86**, 075439 (2012).
- <sup>51</sup> D. S. L. Abergel and V. I. Fal'ko, Phys. Rev. B **75**, 155430 (2007).
- <sup>52</sup> M. Koshino and T. Ando, Solid State Commun. **149**, 1123 (2009).
- <sup>53</sup> L. Zhang, Z. Li, D. Basov, M. Fogler, Z. Hao, and M. Martin, Phys. Rev. B **78**, 235408 (2008).
- <sup>54</sup> A. Kuzmenko, E. van Heumen, D. van der Marel, P. Lerch, P. Blake, K. Novoselov, and A. Geim, Phys. Rev. B **79**, 115441 (2009).
- <sup>55</sup> Z. Li, E. Henriksen, Z. Jiang, Z. Hao, M. C. Martin, P. Kim, H. Stormer, and D. N. Basov, Phys. Rev. Lett. **102**, 37403 (2009).